The Astrophysical Journal, 988:161 (16pp), 2025 August 1 https://doi.org/10.3847/1538-4357/ade052

© 2025. The Author(s). Published by the American Astronomical Society.

OPEN ACCESS

Globular Clusters GMRT Pulsar Search (GCGPS). I. Survey Description, Discovery and Timing of the First Pulsar in NGC6093 (M80)

Jyotirmoy Das[1], Jayanta Roy[1], Paulo C. C. Freire[2], Scott M. Ransom[3], Bhaswati Bhattacharyya[1], Karel Adámek[4], Wes Armour[4], Sanjay Kudale[1,5], and Mekhala V. Muley[5]
[1] National Centre for Radio Astrophysics (NCRA), Pune-411007, Maharashtra, India
[2] Max-Planck-Institut für Radioastronomie (MPIfR), Auf dem Hügel 69-53121, Bonn, Germany
[3] National Radio Astronomy Observatory (NRAO), Charlottesville, VA, USA
[4] Oxford e-Research Centre (OeRC), University of Oxford, Oxford-OX13PJ, UK
[5] Giant Metrewave Radio Telescope (GMRT), Khodad, Pune-410504, Maharashtra, India

Received 2025 February 13; revised 2025 May 2; accepted 2025 May 16; published 2025 July 22

Abstract

This paper describes the new Globular Clusters GMRT Pulsar Search survey. This survey aims to find millisecond pulsars (MSPs) in the globular clusters (GCs) of the Milky Way using the upgraded Giant Metrewave Radio Telescope (uGMRT). Using the uGMRT's Band-4 (550–750 MHz) and Band-3 (300–500 MHz) receivers, this survey will eventually cover the GCs accessible to the uGMRT sky, avoiding GCs visible to the Five-hundred-meter Aperture Spherical Radio Telescope (i.e., $-53° < \delta < -17°$), and targeting GCs that have not been targeted with the sensitivity of this survey. In this paper, we present the discovery and follow-up study of the first pulsar from this survey, J1617–2258A, a 4.32 ms binary MSP, the first to be discovered in the GC NGC 6093. We localized this MSP with arcsecond precision from imaging and obtained the unique timing solution from more than one year of timing observations with the uGMRT Band-4 (550–750 MHz) receivers. This revealed an unusual binary MSP, with a ∼19 hr, highly eccentric ($e \sim 0.54$) orbit having a low-mass companion. This orbital eccentricity allowed the measurement of the rate of advance of the periastron for this system, which led to the derivation of its total mass, $1.67 \pm 0.06\,M_\odot$; this together with the system's mass function implies, for the pulsar and the companion, $M_p < 1.60\,M_\odot$ and $M_c > 0.072\,M_\odot$. The system is most likely a perturbed MSP–helium white dwarf system seen at a low orbital inclination.

Unified Astronomy Thesaurus concepts: Radio astronomy (1338); Globular star clusters (656); Millisecond pulsars (1062); Neutron stars (1108); Surveys (1671); Binary pulsars (153)

1. Introduction

The close interaction of an old neutron star (NS) with a low-mass star results in the formation of low-mass X-ray binaries (LMXBs). In such systems, the NS accretes matter from its companion star and gradually spins up. The high stellar density and high stellar interaction rates (F. Verbunt & P. Hut 1987; D. Pooley et al. 2003; A. Bahramian et al. 2013) found in globular clusters (GCs) allow for the dynamical formation of LMXBs, which is not possible in the Galactic disk, and this is the reason why there are $\sim 10^3$ times more LMXBs per unit mass in GCs compared to the Galactic disk (C. L. Sarazin et al. 2003). At the end of the dynamical evolution of these LMXBs, we are left with pulsars with spin periods of a few milliseconds, called recycled or millisecond pulsars (MSPs, defined here as having $P < 20$ ms and a low B-field; W. Becker & J. Trümper 1999), and a low-mass nondegenerate companion or a low-mass white dwarf (for a review, see T. M. Tauris & E. P. J. van den Heuvel 2023). The large number of LMXBs results in a large number of MSPs: out of the 729 discovered MSPs, 311 are found in GCs.[6]

The local environment of a GC plays an important role not only in the formation of LMXBs and MSPs but also afterward. If the stellar interaction rate per binary, γ (F. Verbunt & P. C. C. Freire 2014), is not very high, the evolution from an LMXB to an MSP is likely to be undisturbed and as a result we are likely to get an MSP with a nondegenerate star as a companion interacting with the MSP (i.e., a spider MSP), or an MSP in a low-eccentricity orbit with a degenerate companion like a white dwarf (WD), i.e., an NS–WD system. These nearly circular systems are indistinguishable from MSPs in the Galactic disk, as observed in lower-density GCs, like M3 (B. Li et al. 2024), M5 (L. Zhang et al. 2023), M13 (L. Wang et al. 2020), and M53 (Y. Lian et al. 2023, 2025).

If γ is very high, then LMXBs might be disrupted to form exotic MSPs, where the end of the accretion results in the formation of mildly recycled, high B-field MSPs (P. C. C. Freire et al. 2011; T. J. Johnson et al. 2013). But even after the accretion ends, interaction with a third stellar object may lead either to the dissociation of the binary system or to the isolation of many pulsars, as observed in core-collapse GCs like Terzan 1 (J. Singleton et al. 2024), NGC 6517 (R. S. Lynch et al. 2011; D. Yin et al. 2024), NGC 6522 (F. Abbate et al. 2023), NGC 6624 (R. S. Lynch et al. 2012; F. Abbate et al. 2022), NGC 6752 (A. Corongiu et al. 2024), and M15 (Y. Wu et al. 2024; D. Zhou et al. 2024). Another event that becomes more likely is the exchange of the low-mass companion of the MSP generally for a more massive one, in what has been designated as a *secondary exchange*. This produces systems like PSR J1807–2500B in NGC 6544

---

[6] Data taken from the ATNF Pulsar Catalogue (https://www.atnf.csiro.au/research/pulsar/psrcat/) and Paulo Freire's GC website (https://www3.mpifr-bonn.mpg.de/staff/pfreire/GCpsr.html).

Original content from this work may be used under the terms of the Creative Commons Attribution 4.0 licence. Any further distribution of this work must maintain attribution to the author(s) and the title of the work, journal citation and DOI.

(R. S. Lynch et al. 2012), PSR J1823–3021G in NGC 6624 (A. Ridolfi et al. 2021), and PSR J1835–3259A in NGC 6652 (M. E. DeCesar et al. 2015), which have no counterparts in the Galactic disk.

For GCs with intermediate densities, like NGC 1851 (P. C. Freire et al. 2004; A. Ridolfi et al. 2022), Terzan 5 (S. M. Ransom et al. 2005; P. V. Padmanabh et al. 2024), and M28 (S. Bogdanov et al. 2011; A. Douglas et al. 2022), we see a mix of both types of populations. Interestingly, some reasonably dense GCs like 47 Tuc (P. C. C. Freire et al. 2017) or M62 (L. Vleeschower et al. 2024) show a "normal" MSP population, only truncated in the orbital period.

The large eccentricities and companion masses of some of the exotic systems make them potentially useful probes of gravitational effects in strong-field regimes—for instance, NGC 1851E might be an MSP–black hole system (E. D. Barr et al. 2024), which would enable tests of new types of gravity theories that until now could not be tested with binary pulsar timing (P. C. C. Freire & N. Wex 2024). Such unusual systems provide a strong motivation for finding additional pulsars in GCs.

Because typical GC distances are of the order of tens of kiloparsecs, most pulsars, which are generally faint radio sources, remain undetected. Indeed, Galactic disk MSPs are typically found within distances of the order of a kiloparsec. This implies two things: (1) the vast majority of GC pulsars remain undetected, meaning many more pulsars in GCs are yet to be discovered, and (2) discovering them will require more sensitive surveys.

Most of the successful and most recent surveys have been conducted in the GHz frequency range, either in the *L* band, like the Parkes and Arecibo GC surveys (carried out around 2000; F. Camilo et al. 2000; A. Possenti et al. 2001, 2005; N. D'Amico et al. 2003; J. W. T. Hessels et al. 2007) and the ongoing Transients and Pulsars with MeerKAT (TRAPUM; A. Ridolfi et al. 2021, 2022) and Five-hundred-meter Aperture Spherical Radio Telescope (FAST; Z. Pan et al. 2021a, 2021b) surveys, or in the *S* band, like the Green Bank Telescope (GBT) *S*-band GC pulsar survey (see S. M. Ransom et al. 2004, 2005; P. C. C. Freire et al. 2008; R. S. Lynch et al. 2011; see also discussion in Section 2); this means that such surveys are biased toward relatively flat-spectrum MSPs. The advent of the upgraded Giant Metrewave Radio Telescope (uGMRT) and its seamless low-frequency coverage (300–850 MHz for uGMRT Band-3 and Band-4) allowed us to use its Y-shaped array and effectively design a pulsar survey to search for GC MSPs in the low-frequency range. Searching GC MSPs with the uGMRT will allow us to discover steep-spectrum GC MSPs that may have been missed earlier due to the bias toward flat-spectrum MSPs in surveys at higher frequencies.

In this paper, we discuss the Globular Clusters GMRT Pulsar Search (GCGPS), from its motivation (Section 2) to its design, sensitivity, and target selection in Section 3. In Section 4, a detailed discussion is presented on the strategy of data analysis. In Section 5.1 we report the first GCGPS discovery, a pulsar in the GC NGC 6093 (also known as Messier 80, henceforth M80), followed by its localization in Section 5.2, profile study in Section 5.3, timing in Section 5.4, and binary properties in Section 5.5; finally we summarize our work in Section 6.

2. Motivation for Designing a GC MSP Search Survey with the uGMRT

The improvement in sensitivity achieved with the uGMRT relative to the legacy GMRT implies the possibility of additional pulsar discoveries. Furthermore, the large number of undiscovered pulsars in GCs and the possibility of finding exotic binaries there that are unlike the Galactic disk pulsars serve as the motivation for this survey.

There are two previously reported GC MSP discoveries with the GMRT. A survey of 10 GCs was made with the legacy GMRT, which resulted in the discovery of the first MSP in NGC 1851, PSR J0514–4002A, a steep-spectrum 5 ms pulsar that is a member of one of the first exotic binaries known that were clearly formed in a secondary exchange encounter (P. C. Freire et al. 2004). The most recent effort was a shallow survey made by T. Gautam et al. (2022), where they discovered the second MSP of NGC 6652, PSR J1835–3259B, an exceptionally young, powerful, and radio-bright system that has a bright, young WD companion (J. Chen et al. 2023) and is one of the three GC pulsars detected in gamma rays (P. Zhang et al. 2022). These surveys, especially the latter, take full advantage of the imaging capabilities of the uGMRT, which have uncovered additional candidates, both in pulsation and in imaging data.

One crucial factor about the existing and ongoing searches for pulsars from GCs is that they mostly focus on GCs that have discovered pulsars in them, as the known dispersion measure (DM) reduces the computational requirements. MeerKAT's TRAPUM and the uGMRT survey by T. Gautam et al. (2022) followed this strategy. Because of this several GCs with no discovered MSPs remained unobserved by sensitive surveys like MeerKAT's TRAPUM or the uGMRT survey; even though GBT and Parkes previously observed some of the GCs, those observations were mostly in GHz frequency (S. M. Ransom et al. 2004, 2005; A. Possenti et al. 2005) and were significantly less sensitive compared to the uGMRT Band-4 (550–750 MHz) central square (CSQ) phased array (PA) beam sensitivity for the same on-source time (discussed in Section 3.3) for steep-spectrum pulsars. The uGMRT's distinctive low-frequency (300–850 MHz for uGMRT Band-3 and Band-4) coverage, particularly Band-4 (550–750 MHz) as discussed in Section 3.1, makes GCs that may have never been searched or have been missed by earlier high-frequency surveys promising targets to search for new MSPs.

Due to FAST's and MeerKAT's superior sensitivity (quantified in Section 3.3), the GCs that remained unobserved by FAST's GC MSP search (*L*-band survey) or MeerKAT's TRAPUM (ultrahigh-frequency (UHF) and *L*-band surveys) make a good set of GCs for which to design an effective survey to search for MSPs with the uGMRT. After careful consideration, we got a significant number of such observable GCs and the majority of them met our additional selection criteria (discussed in Section 3.3), which motivated us to design the GCGPS[7] survey.

3. The Survey

In this section, we will discuss the GCGPS survey details, from the strategic design to the theoretical estimation of the survey sensitivity and target selection.

---

[7] Survey webpage: http://www.ncra.tifr.res.in/~jroy/GC.html.

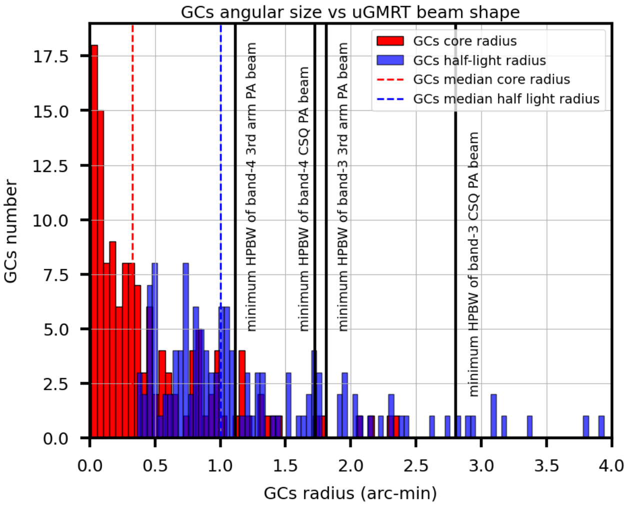

Figure 1. Histogram plot of all the GC core and half-light radii. The vertical dashed red line represents the median core radius value and the similar blue line represents the median half-light radius of all the GCs. All the GC data was taken from W. E. Harris's GC catalog (W. E. Harris 1996, 2010 edition). The four vertical solid black lines represent the uGMRT Band-3 and Band-4 CSQ and third arm PA beams' minimum half-power bandwidth ($\mathrm{HPBW_{min}}$), as marked in the plot.

3.1. Designing the Survey

The uGMRT has 30 antennas distributed in a Y-shaped fashion, with a compact array of 14 antennas at the center within a 1 km^2 area, and the other 16 antennas are distributed in the three arms with a maximum baseline length of ∼28 km to make the array suitable for observing compact objects (G. Swarup et al. 1991; Y. Gupta et al. 2017).

To design this GC MSP search survey effectively for the uGMRT, we need to have an initial estimation of the typical target size for this survey. The known Milky Way GCs have a median core and median half-light radius of $0'.325$ and $1'.0$, respectively (see Figure 1). With this estimation, to select our optimal uGMRT observing band and beam type, using the uGMRT beam simulation code `uGMRT_beam_fov.py`[8] developed for the SPOTLIGHT[9] project, we simulated several types of uGMRT beams and their size variation as a function of elevation for uGMRT Band-3 and Band-4 on NGC 6093 as a reference GC.

Based on the beam simulation results keeping a balance between sensitivity and sky coverage the uGMRT Band-3 and Band-4 CSQ PA beams were the most suitable bands and primary beam type for designing the survey. A PA beam is formed by adding all the antenna voltages coherently preserving the phase information, making the beam narrower but more sensitive than an incoherent array (IA) beam (PA beam sensitivity is $\sqrt{N}$ times the IA beam sensitivity, where N is the number of antennas used to form the beam), which is formed by incoherently adding all the antenna power without the phase information. A CSQ PA beam is a PA beam that is formed only using the closely packed (within 1 km^2) 14 uGMRT CSQ antennas, which is wider than the PA beams formed by adding the long-spaced arm antennas.

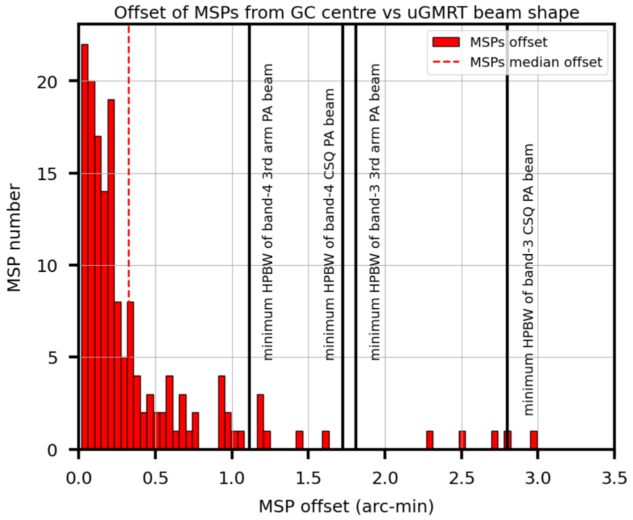

Figure 2. Histogram of the reported position offsets of all GC MSPs from the cluster center. The black solid lines are the same as those in Figure 1.

Statistically, as illustrated in Figure 1, the minimum half-power bandwidth (HPBW) of the Band-4 PA beam exceeds the half-light radius for 77% of the GCs, while for Band-3, the HPBW does so for 92%. We expect to find our MSPs close to the core of the GC. In the observed MSP distribution (as shown in Figure 2), 96% of all the reported localized GC MSPs have a positional offset[10] from the GC center that is less than the minimum HPBW of the uGMRT CSQ Band-4 PA beam and 86% of them have an offset value less than HPBW/2 (indicating they reside in the GC core region). This result is not a selection effect: in most surveys—especially the Parkes and GBT surveys, and the Arecibo searches at lower frequencies—the search beams' HPBWs are larger than $4'$. For Band-3, this coverage is even better, statistically establishing that to observe the whole target GC with optimized sensitivity, the Band-3 or Band-4 CSQ PA beam is sufficient.

Between Band-3 and Band-4, we preferred Band-4 as the first choice due to its lower system temperature (for 650 MHz, $T_{\mathrm{sys}} \sim 102.5$ K) compared to Band-3 (for 400 MHz, $T_{\mathrm{sys}} \sim 130$ K; T. Gautam et al. 2022). Additionally, Band-4 experiences significantly less radio frequency interference (RFI), making it the cleanest band of the uGMRT, whereas Band-3 is more adversely affected by RFI. We used Band-3 only when the target was significantly wider, as it provides better sensitivity coverage compared to Band-4. We excluded Band-5 due to its reduced gain, narrower beam size compared to Band-3 and Band-4, and focus on high-frequency coverage (as discussed in Section 2, low-frequency coverage is preferred).

Along with covering the whole GC with optimum sensitivity, to observe the core with even better sensitivity (where we expected most of our MSPs to be, as we see in Figure 2), we decided to simultaneously form another PA beam including up to the third antenna in each arm (i.e., $N = 22$) called the third arm PA beam. As we can see in Figure 3, due to differences in the baseline length and the number of antennas, the sensitivity of the third arm PA beam is higher than that of the CSQ PA beam (theoretically, number of third arm antennas/number of CSQ antennas = 22/14 ∼ 1.6 times). However, the CSQ beam

---

[8] See https://www.ursi.org/proceedings/RCRS/2024/RCRS2024_0897.pdf.

[9] SPOTLIGHT survey webpage: https://spotlight.ncra.tifr.res.in.

[10] All the MSP position offset data were taken from Paulo Freire's GC website, https://www3.mpifr-bonn.mpg.de/staff/pfreire/GCpsr.html.

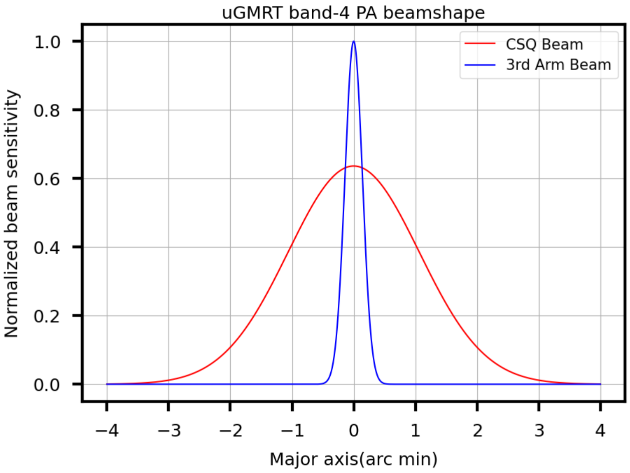

Figure 3. The uGMRT Band-4 CSQ and third arm PA beams' major axis (calculated using `uGMRT_beam_fov.py` for the same initial condition) vs. the normalized beam sensitivity (to the third arm PA beam sensitivity), where it is assumed that the beam sensitivity response is a Gaussian response.

exhibits a wider response compared to the third arm beam. As shown in Figure 1, the uGMRT Band-4 (our primary observing band) CSQ PA beam's minimum HPBW is larger than the half-light radius for approximately 77% of the GCs, enabling full coverage of the GC with optimal sensitivity. Similarly, for the third arm PA beam, around 87% of the GCs have their core radius within the minimum HPBW, providing optimal coverage of the GC core.

An additional advantage of observing a GC simultaneously with two beams (CSQ and third arm) is that, upon detecting a pulsar in the beam data, the signal-to-noise ratio (SNR) between the two beams can immediately provide an estimate of the pulsar's positional offset from the cluster center, using the known beam response from our simulation code. For a pulsar sitting exactly in the beam center, as discussed earlier we would expect the third arm beam SNR to be ∼1.6 times higher than the CSQ beam SNR and this factor will decrease systematically (as shown in Figure 3) with a systematic increase of the position offset from the beam center. With an initial offset estimation, follow-up imaging observations can accurately localize the pulsar in the image plane (see Section 5.2) with minimal effort.

To meet our sensitivity criteria (discussed in Section 3.2), we decided to spend 2.5 hr of observing time on each target. Before the target scan, the entire array is phased on a calibrator to form the PA beam. Instrumental and ionospheric phase perturbations necessitate intermediate phasing every 45 minutes, resulting in two phasing sessions over the observing duration. These prevent dephasing and maintain the PA beam's sensitivity during the entirety of the target scans. This intermediate phasing is done by moving the whole array to a phase calibrator and performing a phasing operation while keeping the beam data recording on. This results in a continuous 2.5 hr beam data set, with 5–10 minutes of phase calibration time every 45 minutes accounting for slewing to the phase calibrator, performing the calibration, and returning to the GCs, which are masked during the analysis.

3.2. Observation Strategy and Sensitivity Coverage

In GCGPS, we primarily used uGMRT Band-4 (550–750 MHz) and for a few wider targets Band-3 (300–500 MHz) as discussed in Section 3.1. For a specific band, the observation strategies employed to achieve optimal target sensitivity are discussed along with the theoretical sensitivity coverage. Given that we are searching for MSPs at mid and low frequencies (with a median GC MSP spin period of 4.60 ms[11]), the sensitivity loss due to pulse broadening from scattering and intrachannel dispersion becomes significant.

According to N. D. R. Bhat et al. (2004), the scatter broadening $W_{\rm scatt}$ in milliseconds is defined as

$$\log[W_{\rm scatt}] = -6.46 + 0.154\log[{\rm DM}] + 1.07\log[{\rm DM}]^2 - 3.86\log[\nu], \quad (1)$$

where DM is the dispersion measure in pc cm^{-3} and ν is the observing frequency in GHz.

According to D. R. Lorimer & M. Kramer (2004), the smearing ($W_{\rm DMintra}$) due to intrachannel dispersion can be defined as (when $\Delta\nu \ll \nu$)

$$W_{\rm DMintra} \simeq 8.3 \times {\rm DM} \times \frac{\Delta\nu}{\nu^3}\,\mu{\rm s}, \quad (2)$$

where $\Delta\nu$ is the channel width/resolution in MHz and ν is the observing frequency in GHz.

While scattering is unavoidable in low-frequency observations, intrachannel dispersion can be eliminated by recording the data in coherently-dedispersed (CD) mode (see T. H. Hankins 1971), provided the GC's DM is precisely known beforehand. By mitigating intrachannel dispersion smearing, this mode enables the recording of high-time-resolution data by reducing the frequency channels in the filterbank output.

The GCs targeted in GCGPS primarily lack known pulsars (as discussed in Section 2), with only a few containing a minimal number of MSPs (discussed in Section 3.3). For GCs with precisely known DMs (i.e., those that have discovered MSPs), we observe with two (CSQ and third arm) simultaneously recorded CD beams (coherently dedispersed at the GC MSPs' median DM) having 512 channels and 40.96 μs sampling time. For GCs with no known DM, we record two (CSQ and third arm) PA beams with 4096 channels and 81.92 μs sampling time.

For each observing mode, the theoretical sensitivity limit can be calculated using the radiometer equation (R. J. Dewey et al. 1985). The minimum detectable flux ($S_{\rm min}$) is defined as

$$S_{\rm min} = \frac{{\rm SNR}\; T_{\rm sys}\;\beta}{GN\sqrt{n_{\rm pol}{\rm BW}_{\rm eff}\Delta t_{\rm obs}}}\sqrt{\frac{W_{\rm eff}}{P_{\rm s} - W_{\rm eff}}}. \quad (3)$$

We define $S_{\rm min}$ as the 10σ (i.e., SNR = 10) detection flux. For 8 bit recording, we assume the digitization loss (β) to be ∼1. For Band-3 at 400 MHz, $T_{\rm sys} \sim 130$ K, whereas for Band-4 at 650 MHz, $T_{\rm sys} \sim 102.5$ K as mentioned earlier in Section 3.1. For the uGMRT, the gain per antenna (G) is about 0.35 K Jy^{-1}. As discussed above, $N = 14$ for CSQ and 22 for the third arm PA beams. For the total intensity Stokes-I data, the number of polarizations ($n_{\rm pol}$) summed up is 2. Our on-source time ($\Delta t_{\rm obs}$) is 2.5 hr for each beamforming observation per target. For Band-3 and Band-4, after eliminating the periodic narrowband RFI-affected channels, the effective bandwidth (BW$_{\rm eff}$) is about 150 MHz and 180 MHz, respectively.

---

[11] Data taken from https://www3.mpifr-bonn.mpg.de/staff/pfreire/GCpsr.html.

Now the effective pulse width can be defined as

$$W_{\rm eff} = \sqrt{W_{\rm int}^2 + W_{\rm DMintra}^2 + W_{\rm scatt}^2 + t_{\rm samp}^2 + W_{\rm DMstep}^2} \qquad (4)$$

where $W_{\rm int}$ is the intrinsic pulse width; $W_{\rm scatt}$ and $W_{\rm DMintra}$ (defined in Equations (1) and (2)) are the intrachannel dispersion smearing and scatter broadening timescale, respectively; and $t_{\rm samp}$ is the smearing that arises due to the finite sampling time. $W_{\rm DMstep}$ is the smearing that arises due to searching the pulsar with a finite DM step; this is calculated for the worst-case scenario, which happens when the pulsar's DM is offset from the search DM by (DM step)/2.

For CD recording $W_{\rm DMintra} = 0$ (if the pulsar is exactly at the DM used to dedisperse the data coherently) and $t_{\rm samp} = 40.96\,\mu$s whereas for PA data $W_{\rm DMintra}$ has a finite value according to Equation (2). For both PA and CD beams, $W_{\rm scatt}$ is the same and calculated using Equation (1) at the center of the band for uGMRT Band-3 and Band-4, which is 0.40 GHz and 0.65 GHz, respectively.

For $W_{\rm DMstep}$, both PA and CD beams will suffer the same smearing. According to D. R. Lorimer & M. Kramer (2004), for our search, the maximum smearing ($W_{\rm DMstep}$) due to the finite DM step can be defined as

$$W_{\rm DMstep} = (8.3 \times 10^6) \times \left(\frac{\rm DM\ step}{2}\right)\left(\frac{1}{f_1^2} - \frac{1}{f_2^2}\right) {\rm ms}, \qquad (5)$$

where f_1 and f_2 are the lowest and highest frequencies of the respective band in MHz, which are 300 MHz and 500 MHz for uGMRT Band-3 and 550 MHz and 750 MHz for uGMRT Band-4, respectively. We take the DM step to be 0.05 pc cm^{-3} for Band-3 and 0.1 pc cm^{-3} for Band-4 according to our DM plan (which is the maximum DM step for the respective band; see Section 4).

For sensitivity analysis, we use an intrinsic pulse width ($W_{\rm int}$) of 10% of the pulse period ($P_{\rm s}$) and DM = 50 pc cm^{-3}, which is a reasonable estimation for a low-frequency MSP survey like GCGPS. Figure 4 shows the detection sensitivity for both PA and CD modes for CSQ beams only, at the true pulsar DM (here DM = 50 pc cm^{-3}) as well as for detections with the maximum DM offset of DM step/2, for both uGMRT bands, as a function of pulsar spin period ($P_{\rm s}$). For the third arm beam, for every observing mode, these sensitivities will scale down (i.e., be more sensitive) by a factor of ∼1.6 (as it scales as $N_2/N_1 = 22/14$; see Section 3.1).

We present the theoretical 10σ detection flux for the GCGPS survey for different observation modes for a 4.60 ms MSP (median spin period of all GC pulsars) with a DM value of 50 pc cm^{-3} for both uGMRT bands when the pulsar was detected at its true DM, in Table 1. The maximum sensitivity loss for the search with a finite DM step for Band-3 (DM step = 0.05 pc cm^{-3}) is ∼2 times and that for Band-4 (DM step = 0.1 pc cm^{-3}) is ∼1.3 times (for the same 4.60 ms candidate period) as compared to the sensitivity (detection at the true DM) we quote in Table 1 (for reference see Figure 4).

3.3. Target Selection

As discussed in Section 2, currently the most prominent ongoing GC search surveys are MeerKAT's TRAPUM and FAST's GC survey. According to A. Ridolfi et al. (2022), for 2 hr of on-source time, the minimum detectable flux (10σ) is 14 μJy and 10 μJy for MeerKAT's UHF band (544–1087 MHz) and *L*-band (856–1711 MHz), respectively. In contrast, according to Z. Pan et al. (2021a), the minimum detectable flux for FAST's *L*-band (1.0–1.5 GHz) survey is 0.76 μJy (same on-source time and detection limit). Assuming the pulsar spectral index is −2, the TRAPUM *L*-band (the most used band) scaled sensitivity at 650 MHz (uGMRT Band-4) is ∼39 μJy, and for FAST the value is about 2.81 μJy. Now from A. Ridolfi et al. (2022), for the same on-source time (2 hr), duty cycle (8%), and DM (52 pc cm^{-3}) and assuming the pulsar period is about 10 ms, the GCGPS primary beam (Band-4 CSQ PA beam) theoretical 10σ sensitivity limit is about 36 μJy.

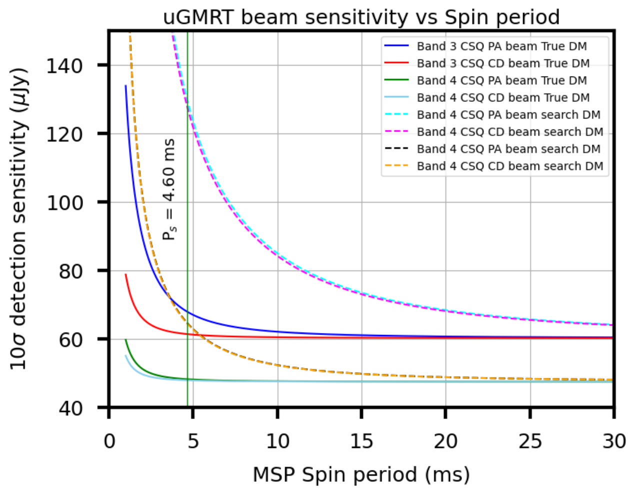

Figure 4. The uGMRT 10σ detection sensitivity (in μJy) vs. the spin period of the observed pulsar for both uGMRT bands' CD and PA modes for the CSQ beam only. For each observing mode, the true DM sensitivity represents the case where one search DM value corresponds exactly to the pulsar's DM (DM*, which in the calculations above is 50 pc cm^{-3}). The search DM sensitivity corresponds to the case where the search DM is DM* + DM step/2, where we will have maximum sensitivity loss due to dispersion smearing caused by the finite DM step used in the search. For uGMRT Band-3 and Band-4, the DM steps are 0.05 and 0.1 pc cm^{-3}, respectively. The sensitivity is calculated using the radiometer equation (refer to Equation (3)) for a pulsar with a 10% duty cycle. The black vertical line represents the sensitivity achieved for the pulsar with the median spin period of all the GC MSPs, where in Band-3 the DM step smearing introduces a maximum reduction of theoretical sensitivity by a factor of ∼2; this factor is ∼1.3 for Band-4.

Given that the FAST GC project follows observing GCs independently of the fact of their having discovered MSPs in them, along with its superior sensitivity compared to the GCGPS survey, we completely excluded GCs that can be observed by FAST (i.e., $\delta > -17°$) from our survey. Also, due to the comparable sensitivity of MeerKAT's TRAPUM for pulsars having a high spectral index, we excluded GCs that MeerKAT had already observed. Now the remaining GCs were the GCs visible to the uGMRT within the decl. range $-53° < \delta < -17°$ ($\delta > -53°$ is the uGMRT sky coverage to have at least 2 hr of target on-source time) and not observed under the TRAPUM project.

Most of the remaining GCs had no prior reported MSP search observations, while a subset had been previously observed with GBT's 2 GHz survey or Parkes's 1.4 GHz GC survey. Assuming an MSP spectral index of −2 (with the GBT 2 GHz and Parkes 1.4 GHz sensitivities scaled to uGMRT Band-4 at 650 GHz), for the same on-source time the

Table 1
Sensitivity Estimation of GCGPS Survey Using the Radiometer Equation by R. J. Dewey et al. (1985), for All the GCGPS Observing Modes and Bands with the Typical On-source Time per Target

On-source Time (hr)	Spin Period (ms)	uGMRT Band (Band-3/Band-4)	uGMRT Array (BM1/BM2)	Beam Type (PA/CD)	Sampling (μs)	# of Channels	S_{min} (10σ) (μJy)
2.5	4.60	Band-3	BM1 (CSQ)	PA	81.92	4096	68
…	…	…	…	CD	40.96	512	61
…	…	…	BM2 (Third Arm)	PA	81.92	4096	43
…	…	…	…	CD	40.96	512	39
…	…	Band-4	BM1 (CSQ)	PA	81.92	4096	48
…	…	…	…	CD	40.96	512	47
…	…	…	BM2 (Third Arm)	PA	81.92	4096	30
…	…	…	…	CD	40.96	512	30

Note. The notations BM1 and BM2 represent the two beams used under this survey (for reference see Table 2). The presented estimated sensitivity is calculated for the median spin period of all the GC MSPs (median $P_s = 4.60$ ms), for a DM value of 50 pc cm^{-3} with a duty cycle of 10%. S_{min} represents the 10σ minimum detection sensitivity for the pulsar detected in the search at the true pulsar DM.

theoretical sensitivity of GCGPS is approximately 3 times better than that of GBT and about 8 times better than that of the Parkes survey. Therefore, we considered observations of the GBT and Parkes observed GCs in the GCGPS (uGMRT Band-3 and Band-4) frequencies.

Figure 5 illustrates significant sensitivity loss in both Band-3 and Band-4, primarily for DM smearing due to the finite search DM step, along with intrachannel dispersion and scattering at higher DMs. However, Band-4 maintains moderate sensitivity even at higher DMs, which was one of our key reasons for selecting it as our primary observing band over Band-3. To account for this sensitivity loss, from the remaining GCs, we chose targets with known or predicted maximum DMs of ~250 pc cm^{-3} for Band-4. For broader targets requiring Band-3 observations, the maximum DM (known or predicted) was limited to less than 100 pc cm^{-3}. We also note that the scatter broadening timescale predicted by Equation (1) does not account for the possibility that GCs, being located at higher Galactic latitudes, may experience reduced scattering even for distant sources with higher DMs. This results in shorter scattering timescales observed for GC pulsars compared to field pulsars with equivalent DMs (Q. He & X. Shi 2024). This will result in sensitivity loss even lower than the value we got using Equations (1), (2), (3), (4), and (5).

Finally, as MSPs can be a prominent source of X-ray/gamma-ray emissions (L. Zhang & K. S. Cheng 2003; P. C. C. Freire et al. 2011; T. J. Johnson et al. 2013; P. Zhang et al. 2022), we ranked the GCs based on their reported X-ray/gamma-ray brightness from different high-energy surveys (N. A. Webb et al. 2006; A. A. Abdo et al. 2010; P. H. T. Tam et al. 2011; P.-H. T. Tam et al. 2016). GCs without any discovered pulsars but exhibiting very high gamma-ray brightness are ideal targets for our survey. Compactness and higher total mass were also considered to prioritize the GC observations. We also assigned lower priority to GCs located more than ~15 kpc away or with a half-light radius exceeding twice the HPBW of the uGMRT CSQ PA beam. After applying these criteria, 31 GCs were identified as optimal candidates for the GCGPS survey. In Table 2, we present these 31 GCs with their relevant information, which will be observed (over multiple uGMRT cycles) under GCGPS. In Table 2, we also present the expected observing mode for each GC, which was decided based on the discussion presented in Section 3.2.

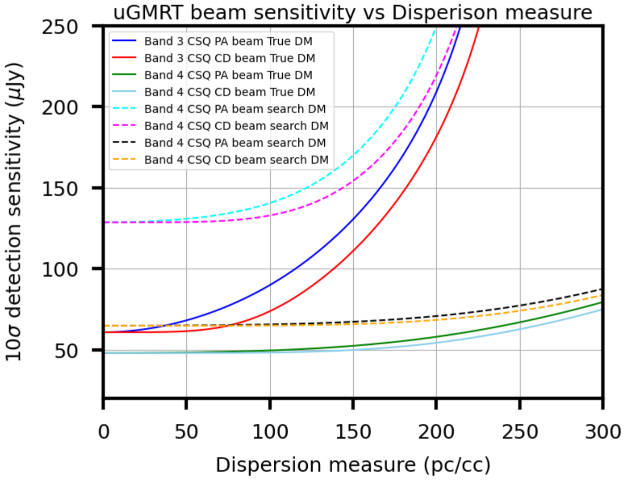

Figure 5. Plot representing the uGMRT 10σ detection sensitivity vs. the DM variation for a fixed pulsar period and duty cycle of 4.60 ms (median spin period of all GC MSPs) and 10%, respectively, for PA and CD data for both uGMRT bands for CSQ beams only in different colors. The sensitivities at the true and search DMs differ in a similar way as seen in Figure 4. The Band-3 CSQ beam is the most affected band with a high DM, and DM smearing (due to a finite search DM step) as well, whereas Band-4 is comparatively better in high DMs.

We note that we are planning to include the GCs observed with MeerKAT in our survey in the near future. This will be facilitated by the improved sensitivity and sky coverage offered by the multibeam formation using the full uGMRT array, utilizing all 30 antennas instead of the single-beam formation by the 14 antennas, which is currently in use in GCGPS. The key enabler of this enhancement is the SPOTLIGHT backend,[12] which allows target-specific multibeam formation with a maximum of 200 postcorrelation beams.[13],[14] Additionally, we will deploy the in-field phasing technique developed by S. Kudale et al. (2024), ensuring that the highly sensitive PA beam (formed using all 30 antennas) maintains its sensitivity over long on-source time. These advancements will enhance our survey sensitivity by a factor of 2–3 for uGMRT

---

[12] For relevant information about the SPOTLIGHT project, see https://spotlight.ncra.tifr.res.in.

[13] See https://www.ursi.org/proceedings/RCRS/2024/RCRS2024_0803.pdf.

[14] See https://www.ursi.org/proceedings/RCRS/2024/RCRS2024_1101.pdf.

Table 2
List of Target GCs of the GCGPS Survey Based on the Selection Criteria Listed in the Text

GC Name (NGC XXXX)	R.A. (J2000) (hh mm ss)	Decl. (J2000) (deg arcmin arcsec)	Core Radius (arcmin)	Half-light Radius (arcmin)	Distance R_{SUN} (kpc)	GC DM (pc cm^{-3})	Expected Observing Mode
NGC 1904	05 24 11.09	−24 31 29.0	0.16	0.65	12.9	53.1*	PA (BM1, BM2)-4
NGC 4590	12 39 27.98	−26 44 38.6	0.58	1.51	10.3	50.3*	PA (BM1, BM2)-4
NGC 5286	13 46 26.81	−51 22 27.3	0.28	0.73	11.7	146.3*	PA (BM1, BM2)-4
NGC 5897	15 17 24.50	−21 00 37.0	1.40	2.06	12.5	48.6*	PA (BM1, BM2)-3
NGC 5986	15 46 03.00	−37 47 11.1	0.47	0.98	10.4	92.17	CD (BM1, BM2)-4
NGC 6093	16 17 02.41	−22 58 33.9	0.15	0.61	10.0	75.2*	PA (BM1, BM2)-4
NGC 6121	16 23 35.22	−26 31 32.7	1.16	4.33	2.2	62.86	CD (BM1, BM2)-3
NGC 6139	16 27 40.37	−38 50 55.5	0.15	0.85	10.1	166.6*	PA (BM1, BM2)-4
NGC 6273	17 02 37.80	−26 16 04.7	0.43	1.32	8.8	125.9*	PA (BM1, BM2)-4
NGC 6284	17 04 28.51	−24 45 53.5	0.07	0.66	15.3	142.5*	PA (BM1, BM2)-4
NGC 6287	17 05 09.13	−22 42 30.1	0.29	0.74	9.4	115.4*	PA (BM1, BM2)-4
NGC 6293	17 10 10.20	−26 34 55.5	0.05	0.89	9.5	146.4*	PA (BM1, BM2)-4
NGC 6304	17 14 32.25	−29 27 43.3	0.21	1.42	5.9	153.3*	PA (BM1, BM2)-4
NGC 6316	17 16 37.30	−28 08 24.4	0.17	0.65	10.4	186.1*	PA (BM1, BM2)-4
NGC 6333	17 19 11.26	−18 30 57.4	0.45	0.96	7.9	114.2*	PA (BM1, BM2)-4
NGC 6342	17 21 10.08	−19 35 14.7	0.05	0.73	8.5	122.4*	PA (BM1, BM2)-4
NGC 6355	17 23 58.59	−26 21 12.3	0.05	0.88	9.2	182.6*	PA (BM1, BM2)-4
NGC 6356	17 23 34.93	−17 48 46.9	0.24	0.81	15.1	144.4*	PA (BM1, BM2)-4
NGC 6388	17 36 17.23	−44 44 07.8	0.12	0.52	9.9	171.4*	PA (BM1, BM2)-4
NGC 6528	18 04 49.64	−30 03 22.6	0.13	0.38	7.9	206.9*	PA (BM1, BM2)-4
NGC 6541	18 08 02.36	−43 42 53.6	0.18	1.06	7.5	108.4*	PA (BM1, BM2)-4
NGC 6553	18 09 17.60	−25 54 31.3	0.53	1.03	6.0	227.3*	PA (BM1, BM2)-4
NGC 6569	18 13 38.80	−31 49 36.8	0.35	0.80	10.9	175.7*	PA (BM1, BM2)-4
NGC 6637	18 31 23.10	−32 20 53.1	0.33	0.84	8.8	119.8*	PA (BM1, BM2)-4
NGC 6638	18 30 56.10	−25 29 50.9	0.22	0.51	9.4	155.5*	PA (BM1, BM2)-4
NGC 6642	18 31 54.10	−23 28 30.7	0.10	0.73	8.1	155.8*	PA (BM1, BM2)-4
NGC 6652	18 35 45.63	−32 59 26.6	0.10	0.48	10.0	116.6*	PA (BM1, BM2)-4
NGC 6681	18 43 12.76	−32 17 31.6	0.03	0.71	9.0	105.2*	PA (BM1, BM2)-4
NGC 6717	18 55 06.04	−22 42 05.3	0.08	0.68	7.1	103.3*	PA (BM1, BM2)-4
NGC 6723	18 59 33.15	−36 37 56.1	0.83	1.53	8.7	82.0*	PA (BM1, BM2)-4
NGC 6809	19 39 59.71	−30 57 53.1	1.80	2.83	5.4	56.7*	PA (BM1, BM2)-3

Note. All relevant values are taken from the W. E. Harris list of GC parameters (W. E. Harris 1996, 2010 edition). R_{SUN} is the GC distance from the Sun. The DM values in the second-to-last column of the table represent either the median DM of all the MSPs in that particular GC (GCs with already known MSPs) or for GCs with no known pulsars the DM predicted by the YMW16 model (J. M. Yao et al. 2017; marked with "*"). The last column represents the expected observing mode for each GC, which we decided based on the GC parameters—where PA and CD are the beam type, BM1 and BM2 are the CSQ and third arm beams, and the two numbers (3 and 4) represent the two uGMRT observing bands (Band-3 and Band-4, respectively).

Band-3 and Band-4, as compared to the current sensitivity of GCGPS.

This will enable us to observe all low-DM GCs (DM $<$ 250 pc cm^{-3}) seamlessly within the declination range $-53° < \delta < -17°$.

In this paper, we present the discovery of the first MSP in NGC 6093 from GCGPS, along with its timing studies. A comprehensive list of already GCGPS-observed GCs from Table 2, including all discoveries and nondetection limits, will be detailed in future publications.

4. Data Analysis

The PA beam data recorded from the uGMRT Wideband Backend (S. H. Reddy et al. 2017) was initially processed to mitigate RFI signals and to correct instrumental effects, such as slopes in the bandpass. We used `GPTOOL`[15] to eliminate RFI signals exceeding the threshold value along both the time and frequency axes, as well as to normalize the band shape. The bandpass-corrected filtered beam data was then converted to the `SIGPROC`[16] filterbank format for further processing. We developed an end-to-end `PRESTO`[17] based pulsar search pipeline called `PulsarSearchScript` (PSS), which is available on GitHub.[18] This pipeline is integrated with a candidate sifting code, enabling the reduction of the huge number of candidates (based on some thresholds and grouping criteria discussed below) to search for pulsars efficiently. We used the pulsars discovered by the GHRSS survey (B. Bhattacharyya et al. 2016, 2019) to test and optimize the PSS pipeline used in GCGPS.

For the observed GCs that already had discovered pulsars, for both uGMRT bands (Band-3 and Band-4), we searched within the range of median DM $= \pm 15$ pc cm^{-3} with a DM step of 0.02 pc cm^{-3}, resulting in a total of 1500 DM trials, while having negligible additional sensitivity loss due to the search with a finite DM step size, and no intrachannel dispersion sensitivity loss also due to CD data. After dedispersion, we performed a fast Fourier transform on the dedispersed data, followed by an acceleration search with a $\pm 200(z_{\max})$ bin drift correction to account for the Doppler-shifted period caused by the line-of-sight acceleration of a binary system.

After the acceleration search, to reduce the enormous number of candidates, we applied a DM clustering filter in our candidate sifting code. To optimize our sifting code, we defined the DM clustering threshold for each band based on a worst-case scenario: a candidate with a 1 ms period and a 5σ detection significance, representing the lower limits of our search parameter space. Based on tests using true pulsar data from the GHRSS survey, we adopted a conservative assumption that such signals remain detectable within ± 0.05 pc cm^{-3} for Band-3 and ± 0.15 pc cm^{-3} for Band-4 of their true DM values. Beyond these ranges, dispersion smearing causes the signal to become undetectable in `PRESTO`'s acceleration search. This sets the total DM span for clustering to 0.1 pc cm^{-3} for Band-3 and 0.3 pc cm^{-3} for Band-4. For both uGMRT bands, these spans define the minimum DM space a real pulsar should occupy with a period of 1 ms and a detection significance of 5σ. Candidates with longer periods or higher SNRs are less affected by smearing and are expected to meet these thresholds easily. For GCs with known MSPs (i.e., known DMs), the clustering threshold for uGMRT Band-4 is set to 15, based on a DM step size of 0.02 pc cm^{-3} and a total clustering span of 0.3 pc cm^{-3} (i.e., 0.3/0.02). So, for Band-4, for the DM step 0.02 pc cm^{-3}, a candidate has to be present in at least 15 consecutive DM trials to qualify for further analysis. Similarly, for Band-3, we followed the same approach using the defined band-specific DM step size and DM span. The upper periodicity limit was set to 10 s.

After this sifting, we were left with a manageable number of candidates, yet made sure we did not miss any true pulsar candidates. Now we folded these candidates over the frequency and time domains using `PRESTO`'s `prepfold`. Then, manual inspections were conducted over these folded profiles to check for the presence of any periodic signals in both time and frequency domains.

To process the data from GCs without any discovered pulsars, we initially used both the NE2001 (J. M. Cordes & T. J. W. Lazio 2002) and YMW16 (J. M. Yao et al. 2017) models to predict the GC DM and optimize our DM search range. Testing both models on GCs with known DMs revealed that both tend to overpredict the GC DM at the given GC distance. However, in most cases, the YMW16 model provided DM predictions closer to the actual values compared to the NE2001 model. In the worst-case scenario, the YMW16 model predicted the DM was a factor of 1.5–2 higher than the GC DM. This observation led us to use the YMW16 model over the NE2001 to predict the DM values for further analysis.

Using the predicted DM value (DM*), we searched over the DM space as given below (optimizing computational cost):

$$\frac{1}{3}\mathrm{DM}^* \leqslant \mathrm{DM} \leqslant \frac{3}{2}\mathrm{DM}^*, \tag{6}$$

or

$$\mathrm{DM} = \mathrm{DM}^* \pm 50\ \mathrm{pc\ cm^{-3}}. \tag{7}$$

We chose our DM space according to Equation (6) or (7), whichever probes a larger DM range. As shown in Equation (6), for larger predicted DM values, the DM search range is biased toward lower DMs rather than higher DMs due to the overpredictive nature of the YMW16 model. For GCs with no pulsars, we used a DM step of 0.05 pc cm^{-3} and 0.1 pc cm^{-3} for uGMRT Band-3 and Band-4, respectively, optimizing the computational costs while keeping a manageable sensitivity loss for smearing due to a search with a finite DM step size. After dedispersion and an acceleration search, we applied the candidate sifting approach as discussed earlier. We processed the data through PSS using this DM plan, applying a 5σ candidate detection threshold, the appropriate DM clustering threshold (as outlined earlier in this section), and period cutoffs of 1 ms and 10 s. The filtered candidates were then folded and manually inspected for the presence of periodic signals in time and frequency space. These search strategies were systematically applied to all of our GCGPS data.

5. First Pulsar Detected in NGC 6093 (M80)

5.1. Discovery

Under GCGPS, in 2023 July we observed NGC 6093, using the uGMRT Band-4 CSQ and third arm PA beams simultaneously. At first, we performed the search on the CSQ data having a wider beam response, using the YMW16 predicted value for NGC 6093 (DM$^* \sim 75.2$ pc cm^{-3}), following Equation (7) over the DM range of 25–125 pc cm^{-3}, with DM step 0.1 pc cm^{-3}. During the manual inspection of the folded profiles in the search output, we identified an MSP at a period of 4.32 ms with a DM of 66.9 pc cm^{-3}. With 2.5 hr of on-source time, the CSQ beam resulted in a detection SNR of 16.3σ, whereas the third arm beam folding for this MSP (with the known period, period

---

[15] See https://github.com/chowdhuryaditya/gptool.

[16] See https://sigproc.sourceforge.net/.

[17] PRESTO GitHub page: https://github.com/scottransom/presto.

[18] See https://github.com/jyotirmoydas5392/Pulsar_Search_Script.

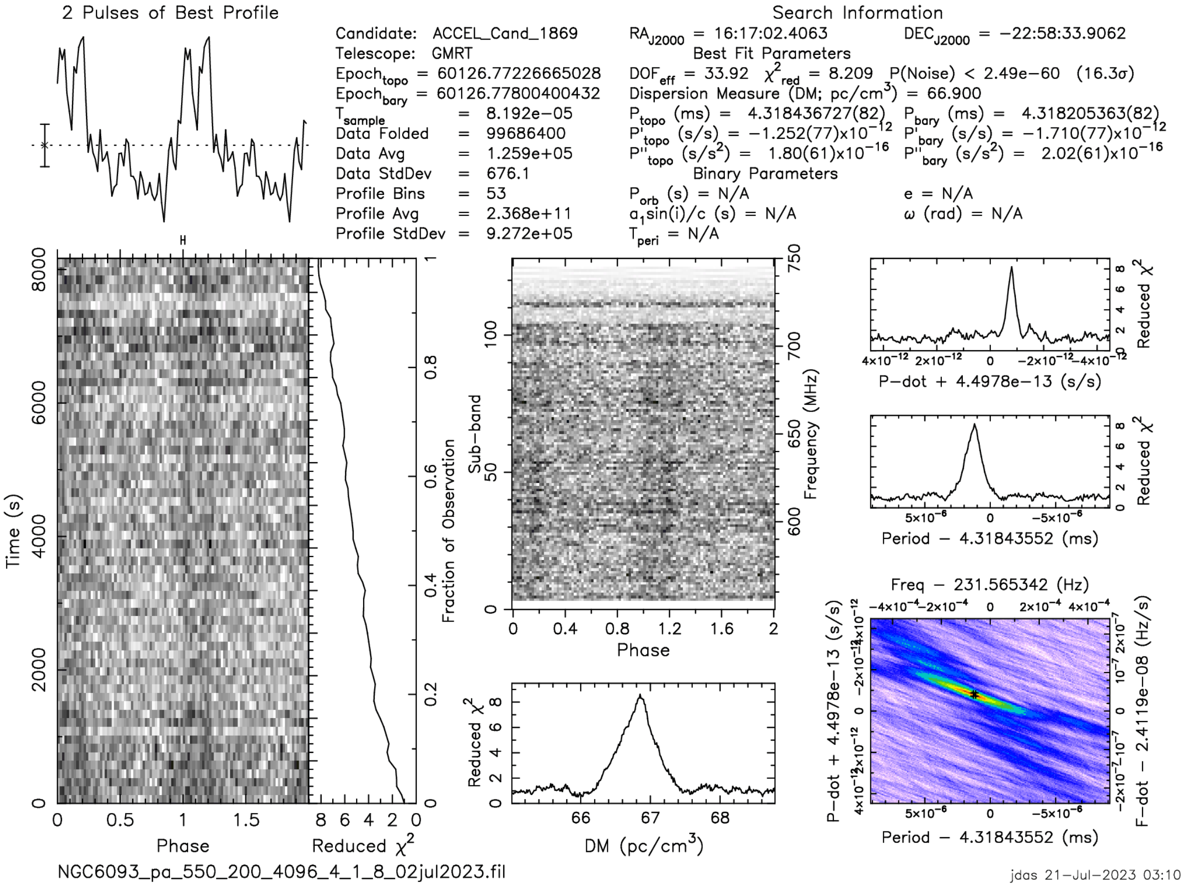

Search Information

Candidate: ACCEL_Cand_1869

Telescope: GMRT

$\mathrm{Epoch_{topo}}$ = 60126.77226665028

$\mathrm{Epoch_{bary}}$ = 60126.77800400432

$\mathrm{T_{sample}}$ = 8.192e−05

Data Folded = 99686400

Data Avg = 1.259e+05

Data StdDev = 676.1

Profile Bins = 53

Profile Avg = 2.368e+11

Profile StdDev = 9.272e+05

$\mathrm{RA_{J2000}}$ = 16:17:02.4063 $\mathrm{DEC_{J2000}}$ = −22:58:33.9062

Best Fit Parameters

$\mathrm{DOF_{eff}}$ = 33.92 χ^2_{red} = 8.209 P(Noise) < 2.49e−60 (16.3σ)

Dispersion Measure (DM; pc/cm^3) = 66.900

$\mathrm{P_{topo}}$ (ms) = 4.318436727(82) $\mathrm{P_{bary}}$ (ms) = 4.318205363(82)

$\mathrm{P'_{topo}}$ (s/s) = $-1.252(77)\times10^{-12}$ $\mathrm{P'_{bary}}$ (s/s) = $-1.710(77)\times10^{-12}$

$\mathrm{P''_{topo}}$ (s/s^2) = $1.80(61)\times10^{-16}$ $\mathrm{P''_{bary}}$ (s/s^2) = $2.02(61)\times10^{-16}$

Binary Parameters

$\mathrm{P_{orb}}$ (s) = N/A e = N/A

$a_1\sin(i)/c$ (s) = N/A ω (rad) = N/A

$\mathrm{T_{peri}}$ = N/A

Figure 6. The discovery `PRESTO` output plot of J1617–2258A, the first MSP of NGC 6093. The time vs. phase and frequency vs. phase output are presented in gray scale.

derivative, and DM a priori from the CSQ detection) yielded a detection significance of 6.3σ. This difference in SNR suggests a positional offset of the MSP from the cluster center (details in Section 5.2). In this region, the sensitivity of the third arm beam decreases rapidly, whereas the wider CSQ beam maintains moderate sensitivity, allowing better coverage. In Figure 6, we present the discovery folded profile plot of J1617–2258A (the first pulsar of M80), from the standard `PRESTO` folding output.

5.2. Localization

In the GCGPS observations, simultaneously with the beam recording we also recorded the interferometric data with a time integration of 5.3 s for imaging analysis of the field. The imaging was done using the automated pipeline (called CAPTURE; R. Kale & C. H. Ishwara-Chandra 2021) developed for the uGMRT data. For the M80 observations, we observed 3C 48 as the amplitude calibrator, and 1830–360 was observed every 40 minutes of the target scan (the scan of NGC 6093) as a phase calibrator.

The uGMRT interferometric imaging for 2.2 hr of integration time on M80 resulted in an rms noise of $\sim$20 μJy. Imaging of the field revealed four sources within a $1\overset{\prime}{.}5$ radius from the cluster center. The first source (the source visible in Figure 7) was $\sim 6\overset{\prime\prime}{.}5$ off from the cluster center where the discovery beam was formed. The approximate distance of the source was calculated using the SNR ratio of both beams (see Section 5.1) and the beam simulation code `uGMRT_beam_fov.py` (see Section 3.1). We simulated the Band-4 CSQ and third arm PA beams for the time of observation to determine the offset from the beam center. The simulation indicates that the source is located within approximately 10$''$ of the cluster center. Now the source with a $\sim 6\overset{\prime\prime}{.}5$ offset from the cluster center and an imaging estimated flux of 350 ± 25 μJy was considered as the primary target as the position of the pulsar.

To verify this position estimate, we observed NGC 6093 using both the CSQ and third arm PA beams, centered on the probable pulsar location (i.e., on the source, $\sim 6\overset{\prime\prime}{.}5$ off from the cluster center). For 1.5 hr of on-source time, the CSQ and third arm PA beam detection significance was 12.2σ and 17.3σ, respectively (i.e., third arm SNR to CSQ SNR ratio $\sim$ 1.42). Now for the pulsar to be localized, the expected SNR ratio is $\sim$1.6 (see Figure 3 and discussion in Section 3.1). We note that a theoretical and observed SNR ratio difference may arise due to multiple factors like the phasing efficiency, number of available antennas, RFI condition for both beams, etc. Therefore, we identified this radio source as J1617–2258A and proceeded with timing follow-up to enhance astrometric precision.

More than one year of timing follow-up of J1617–2258A allowed us to obtain a phase-coherent timing solution

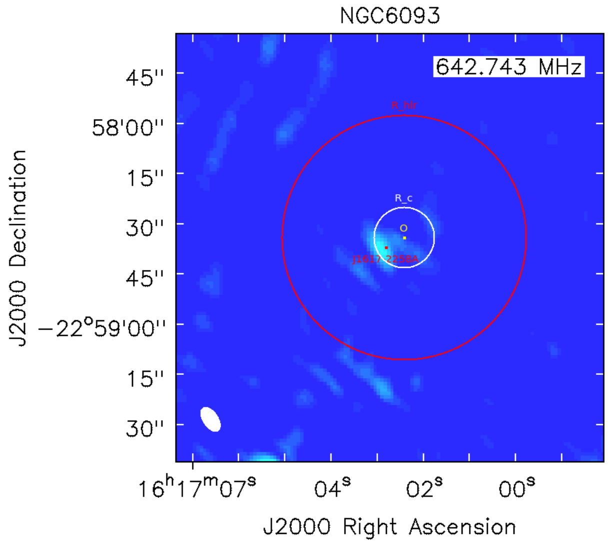

Figure 7. The uGMRT Band-4 (f_c = 650 MHz) image of M80 using the CAPTURE pipeline. The image was produced from the simultaneous recording of the beam data during the beamforming discovery observation. The yellow and red circles represent the core radius and the half-light radius of M80, respectively. The point marked with "O" is the GC center and the position of J1617–2258A obtained from the timing analysis is marked with "A," which sits inside the core radius on the lower left side.

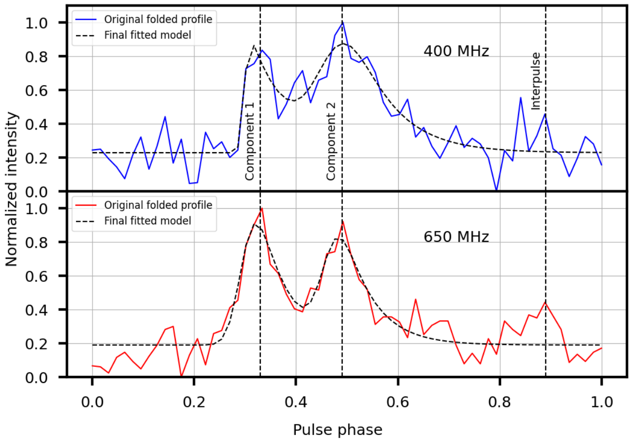

Figure 8. The CD folded profile of J1617–2258A for uGMRT Band-3 (f_c = 400 MHz) and Band-4 (f_c = 650 MHz). For Band-4, the sampling was 10.24 μs and for Band-3, the sampling was 40.96 μs and both foldings in the plot are downsampled to 64 bins for better visualization. The black dashed curve represents the best-fit profile according to Equation (8).

(discussed in Section 5.4), improving the positional error (1σ) up to 0.″30. The timing position is marked in Figure 7 with the letter "A," which overlaps with the imaging position, confirming that it is J1617–2258A.

5.3. Scattering Timescale and Profile Evolution

The low-frequency high-time-resolution pulse profile, which is unaffected by intrachannel dispersion, was obtained by observing the pulsar in the uGMRT Band-3 CD mode at the MSP DM at 40.96 μs sampling with 1024 channels. The Band-4 CD profile was obtained from the timing observation, where, along with the PA mode (used for timing), we simultaneously observed the MSP in CD mode with 10.24 μs sampling and 512 channels. This allowed us to obtain two (Band-3 and Band-4) CD pulse profiles, with reasonable SNRs for further study. We utilized these CD pulse profiles to characterize the low-frequency profile evolution and determine the scattering timescale.

Table 3
The Scattering Timescale along with the Width of Both Components Obtained from Fitting the CD Data (Data Unaffected by Intrachannel Dedispersion)

Frequency (MHz)	Scattering Width (ms)	Component Number	Intrinsic HPBW (ms)
400	0.328 ± 0.104	1	0.075 ± 0.054
…	…	2	0.416 ± 0.142
650	0.230 ± 0.046	1	0.229 ± 0.037
…	…	2	0.264±0.063

Note. We use the convention used in M. M. McKinnon (2014) to fit our folded pulse profile. For Band-4, the profile time resolution was 10.24 μs, and for Band-3, it was 40.96 μs. The error presented here was obtained from the covariance matrix of the `curve_fit` algorithm.

As we can see in Figure 6 and in Figure 8, the MSP has two clear profile components in both frequencies. It also has a faint interpulse. The pulse profile is broader at 400 MHz compared to 650 MHz, where the two components are more distinctly defined. We followed the approach of M. M. McKinnon (2014) to determine the scattering timescale and intrinsic profile evolution. In this method, we fit the CD pulse profiles, assuming that all components intrinsically follow a Gaussian distribution and share the same scattering timescale at a given frequency. Additionally, since coherent dedispersion was applied, DM smearing is considered negligible. According to M. M. McKinnon (2014), for each profile component, the scattering-broadened model can be defined as

$$f(t,\,\tau) = A + \frac{S}{2\tau}\exp\left(\frac{\sigma^2}{2\tau^2}\right)\times\exp\left(-\frac{(t-\mu)}{\tau}\right) \times\left(1+\mathrm{erf}\left[\frac{t-(\mu+\sigma^2/\tau)}{\sigma\sqrt{2}}\right]\right). \tag{8}$$

Here, A is the constant offset, S is the integrated flux density of the component, μ is the mean, σ is the standard deviation, erf is the error function, and τ is the scattering timescale.

Both bands' (Band-3 and Band-4) CD pulse profile components (except the interpulse) were fitted and the components' intrinsic widths and scattering timescale were determined. For each band, during the fitting of the multiple components, the scattering timescale (τ) was kept fixed, while the components' intrinsic widths (here the components' HPBWs: 2.355 × σ) are independent of each other. The fitting was done using the Python package `curve_fit`.[19]

In Table 3, we summarize the obtained pulse widths and scattering timescales for this MSP in both uGMRT bands. The error we present here is the square root of the diagonal elements of the covariance matrix obtained from the `curve_fit` algorithm to get the independent fitting error of each parameter. As we see in this table (Table 3), for Band-3 (f_c = 400 MHz), the obtained values are not as constrained

---

[19] The package `curve_fit` can be found here: https://docs.scipy.org/doc/scipy/reference/generated/scipy.optimize.curve_fit.html.

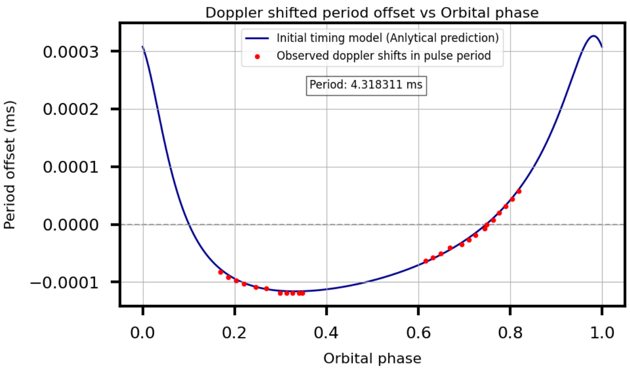

Figure 9. Doppler-shifted period vs. orbital phase. The scattered red points represent the period offsets we got from the detections from the observations (seven epochs) we used for the initial timing, after subtracting the Doppler shift from the Earth's motion (i.e., barycentering). The blue curve represents the best orbital model fit of the observed data produced by `FITORBIT`. We can clearly see the eccentric nature of the orbit, deviating from the sinusoidal prediction for a circular orbit.

as those for Band-4 ($f_c = 650$ MHz), due to the very low SNR detection of the MSP (as can be seen in Figure 8).

Figure 8 shows the average pulse profile for both frequency bands, each defined by its central frequency (f_c). The profile presented here was obtained after binning the data into 64 intervals for enhanced clarity, with the original fitted model of unaveraged data represented by the dashed curve.

5.4. *Timing*

Here, we present a detailed discussion of the pulsar's timing, leading to a phase-coherent timing solution, followed by an analysis of the results obtained from the timing study.

5.4.1. *Deriving the Orbit*

Given the detection with a significant acceleration in the discovery observation, it was clear that it is a binary MSP. To probe the nature of the binary orbit, we followed up on this MSP for seven epochs (including the discovery epoch and one confirmation epoch), with a minimum separation of one day and a maximum separation of one month between two consecutive epochs.

For each epoch, we derived the pulsar period evolution with time and used the timing package `FITORBIT`[20] to fit a Keplerian model to the temporal variation of spin period. In Figure 9 we can see the observed spin periods as a function of orbital phase and the best-fit orbital model derived by `FITORBIT`, where we found that J1617–2258A is in a highly eccentric ($e \sim 0.5374$) relatively compact relativistic orbit having an orbital period (P_b) $\sim$ 18.94 hr, and a projected semimajor axis $x = 0.4642$ s. The mass function of a binary system is given by

$$f(M_p, M_c) = \frac{(M_p \sin i)^3}{(M_p + M_c)^2} = \frac{4\pi^2}{T_\odot}\frac{x^3}{P_b^2} = 1.7247(2) \times 10^{-4}\,M_\odot, \tag{9}$$

where $T_\odot = (\mathcal{GM})^{\rm N}_\odot / c^3 = 4.925490947\,\mu$s is an exact quantity, with the solar mass parameter $(\mathcal{GM})^{\rm N}_\odot$ (A. Prša et al. 2016) in time units. Assuming $M_p = 1.4\,M_\odot$, we obtained minimum ($i = 90°$) and median ($i = 60°$) companion masses of 0.072 $M_\odot$ and 0.084 $M_\odot$, respectively.

Although at this stage the timing model was not well constrained, the large-eccentricity and relatively compact orbit made this a promising system for the precise measurement of multiple relativistic effects in the orbital motion, which will enable mass measurements in the near future.

5.4.2. *Phase Connection and Timing Solution*

To achieve phase connection, we conducted biweekly follow-up observations of J1617–2258A using uGMRT Band-4 (550–750 MHz) on 18 occasions, including the discovery, confirmation, and follow-up epochs, from 2023 July to 2024 August. The timing observations are still ongoing on a monthly cadence. The average detection significance per epoch ranges from 15σ to 30σ depending on the observation duration and phasing efficiency.

We implemented a three-step approach to enhance the precision of the pulse time of arrival (ToA) measurements and refine the timing solution. We began by using `TEMPO`[21] to connect the ToAs of nearby epochs, continuing this process until no further unambiguous connections could be established. At this stage, we derived an improved ephemeris, which was then used to refold all data, refine pulse profile templates, and recompute the ToAs. When no more connections could be made, we used `DRACULA` (P. C. C. Freire & A. Ridolfi 2018). It is a `TEMPO`-based software that iteratively determines the unique solution. Finally, with the new parameter file, we again folded all the epochs, generated relatively fewer ToAs to reduce their uncertainties, and did the final iteration of timing to obtain our unique precise timing model, which is presented in Table 4. This uses the DE440 solar system ephemeris (R. S. Park et al. 2021) to account for the Earth's motion around the solar system barycenter and the "DD" orbital model (T. Damour & N. Deruelle 1986) to describe the pulsar's orbit. Figure 10 represents the postfit residuals, which are the ToA values minus the prediction of the timing solution in Table 4 for the same rotation.

5.4.3. *Position and Spin Parameters*

The precise position of J1617–2258A obtained from the timing (listed in Table 4) coincides with the radio source (as seen in Figure 7) discussed in Section 5.2, confirming its association with J1617–2258A. The pulsar is located $6\farcs44$ from the cluster center defined by E. Vasiliev & H. Baumgardt (2021). This distance represents about 0.72 core radii, where the core radius is assumed to be $\sim 9''$ (see W. E. Harris 1996, 2010 edition). At the distance of M80, about 9.8 kpc (E. Vasiliev & H. Baumgardt 2021), this represents a projected distance of 0.306 pc.

The observed spin period derivative of the pulsar ($\dot{P}_{\rm obs}$) is the sum of the intrinsic spin period derivative ($\dot{P}_{\rm int}$) and contributions from the acceleration of the system in the Galaxy ($a_{\rm Gal}$, from which we subtract the acceleration of the solar system in the Galaxy) and in the GC ($a_{\rm GC}$), both projected along the line of sight to the system, and finally the Shklovskii

---

[20] The GitHub page for the `FITORBIT` package: https://github.com/vivekvenkris/fitorbit.

[21] TEMPO GitHub page: https://github.com/nanograv/tempo.

Table 4
Timing Solution of J1617–2258A

Parameter (Units)	Designation or Value
Parameters of observation and timing solution	
PSR	J1617–2258A
Reference epoch (MJD)	60166.864788
Start of timing data (MJD)	60126.783
End of timing data (MJD)	60508.571
Number of ToAs	34
Postfit timing residuals, rms (μs)	12.137
Solar system ephemeris	DE440
Time units	TDB
Binary model	DD
Measured parameters	
R.A., α (J2000; hh:mm:ss)	16:17:02.821(4)
Decl., δ (J2000; deg:arcmin:arcsec)	–22:58:36.8(3)
Spin frequency, f (Hz)	231.572028561(2)
First spin frequency derivative, $\dot{f}$ (Hz s^{-1})	–3.3(1) × 10^{-15}
DM (pc cm^{-3})	66.812
Orbital period, P_b (days)	0.78914809(7)
Projected semimajor axis, x (lt-s)	0.46421(1)
Eccentricity, e	0.53744(3)
Time of periastron, T_0 (MJD)	60166.84499(2)
Longitude of periastron, ω (deg)	24.703(9)
Rate of periastron advance, $\dot{\omega}$ (deg yr^{-1})	0.5851 ± 0.0149
Derived parameters	
Position offset from GC center (arcsec)	6.444
Position offset from GC center (core radii)	0.72
Spin period, P (ms)	4.318310834921(3)
Spin period derivative, $\dot{P}$ (s s^{-1})	6.1(2) × 10^{-20}
Characteristic age, τ_c (Gyr)	>0.25
Estimated surface magnetic field, B (10^9 G)	<1.1
Mass function, $f(M_p, M_c)$ ($M_\odot$)	0.00017247(2)
Total mass of the system, $M_{\rm tot}$ ($M_\odot$)	1.67 ± 0.06
Minimum companion mass, $M_{\rm c,min}$ ($M_\odot$)	0.07203(3)
Median companion mass, $M_{\rm c,med}$ ($M_\odot$)	0.08361(3)
Maximum pulsar mass, $M_{\rm p,max}$ ($M_\odot$)	1.60 ± 0.06

effect (I. S. Shklovskii 1970), which can be derived from the total proper motion of the system (μ) and its distance (d):

$$\frac{\dot{P}_{\rm obs}}{P} = \frac{\dot{P}_{\rm int}}{P} + \frac{a_{\rm Gal}}{c} + \frac{a_{\rm GC}}{c} + \frac{\mu^2 d}{c}. \tag{10}$$

To calculate $a_{\rm Gal}$, we use the Galactic potential model of P. J. McMillan (2017), which yields $a_{\rm Gal} = -0.409 \times 10^{-9}\,{\rm m\,s^{-2}}$. To calculate the Shklovskii effect, we assume that the proper motion of the pulsar (J1617–2258A) is the same as that of the GC (NGC 6093), which is $\mu_\alpha = -2.934 \pm 0.027\,{\rm mas\,yr^{-1}}$ and $\mu_\delta = -5.578 \pm 0.026\,{\rm mas\,yr^{-1}}$ (E. Vasiliev & H. Baumgardt 2021); this results in an apparent acceleration of $a_{\rm Shk} = \mu^2 d = +0.284 \times 10^{-9}\,{\rm m\,s^{-2}}$. Thus the sum of the kinematic contributions from the Galaxy is $-0.122 \times 10^{-9}\,{\rm m\,s^{-2}}$. From this, we can derive, for $\dot{P}_{\rm int} = 0$, an upper limit of the acceleration of the pulsar in the gravitational field of M80 (projected along the line of sight):

$$\begin{aligned} a_{\rm l,max} &= \frac{\dot{P}_{\rm obs}}{P}c - a_{\rm Gal} - a_{\rm Shk} \\ &= +4.35 \times 10^{-9}\,{\rm m\,s^{-2}}. \end{aligned} \tag{11}$$

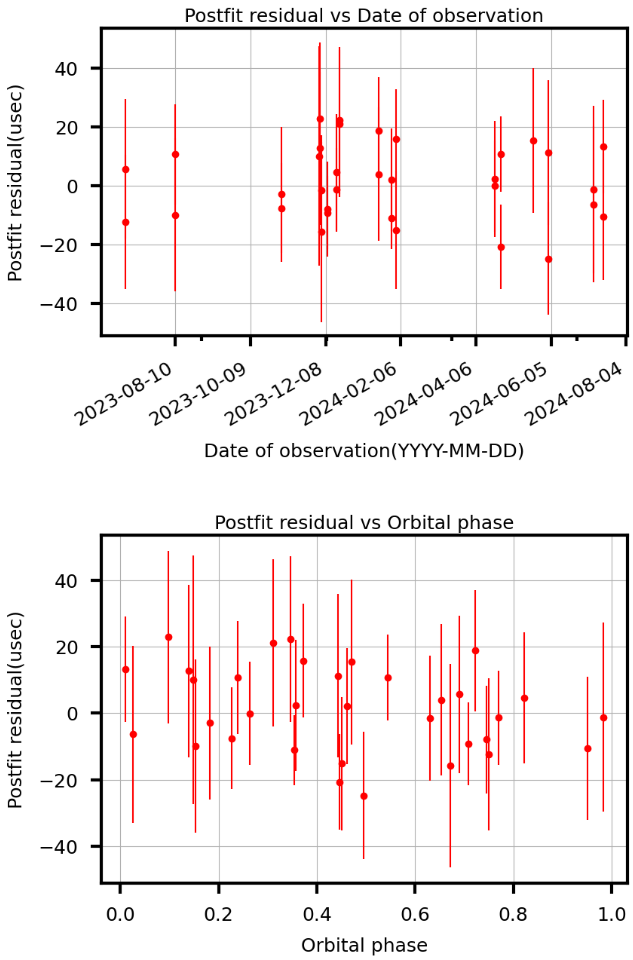

Figure 10. Postfit timing residual vs. epoch (top) and orbital phase (bottom, where the mean anomaly is measured from periastron) after achieving the phase-coherent timing solution. The vertical lines with each point represent the rms error of each ToA.

To model the gravitational field of M80, we use the analytical model described by P. C. C. Freire et al. (2005), where we use a velocity dispersion in the core of $12.4\,{\rm km\,s^{-1}}$ (W. E. Harris 1996, 2010 edition). For the line of sight of the pulsar, this model predicts a maximum/minimum cluster acceleration of $a_{\rm GC} = \pm 14.75 \times 10^{-9}\,{\rm m\,s^{-2}}$, which is significantly larger than the $a_{\rm l,max}$ of the pulsar; this means that the value of $a_{\rm l,max}$ is well within the range of accelerations predicted by our mass model for M80. Assuming the minimum possible cluster acceleration, we obtain an absolute upper limit of $\dot{P}_{\rm int} < 2.75 \times 10^{-19}$. From this value, the limits on characteristic age (τ) and surface magnetic field strength (B) can be estimated using

$$\tau_c = P/2\dot{P},\ \ B = 3.2 \times 10^{19}(P\dot{P})^{1/2}, \tag{12}$$

from which we obtain $\tau_c > 0.25$ Gyr and $B < 1.1 \times 10^9$ G. These values are not very constraining, but they are consistent with the typical values obtained for MSPs in the Galactic disk. Much improved values will be obtained when the orbital period derivative of the system becomes measurable (see, e.g., the discussion in P. C. C. Freire et al. 2017).

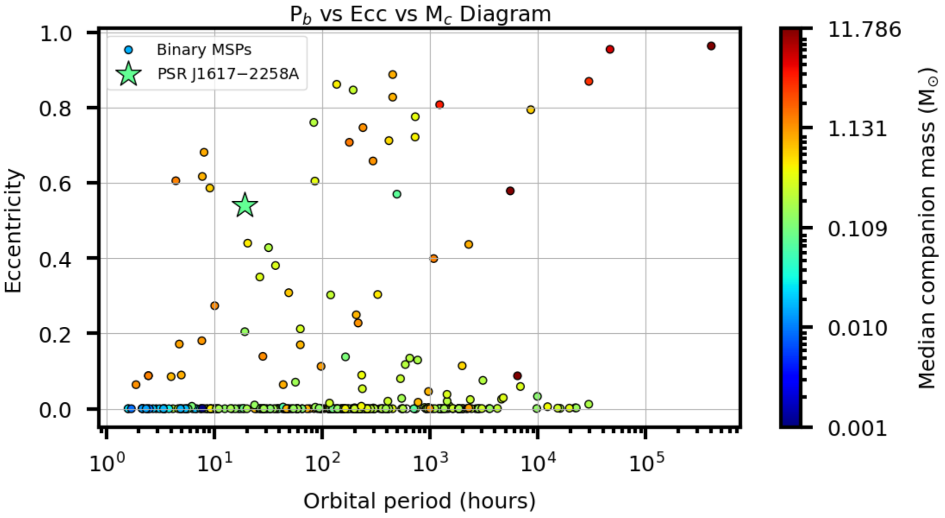

Figure 11. The plot of the orbital period vs. eccentricity for all the binary MSPs detected until now, along with GCGPS's J1617–2258A. All the binary MSP data were taken from the ATNF Pulsar Catalogue (R. N. Manchester et al. 2005). The additional axis is the median companion mass of each system represented as the color of each dot, and the color bar represents the range. As seen in the plot, highly eccentric systems generally have either wide orbits, high-mass companions, or a combination of both. In contrast, the newly discovered GC MSP J1617–2258A, having a compact orbit and a companion with low median mass, is quite eccentric and sits in a unique spot in the plot. Only four systems are more eccentric while having a more compact orbit, but interestingly, all of them have median companion masses higher than J1617–2258A.

5.5. Binary Characteristics

In this section, we discuss the binary characteristics of J1617–2258A, the unique compact eccentric orbit and its companion type.

5.5.1. The Compact Eccentric Orbit of J1617–2258A

The evolution of LMXBs greatly shapes the resultant MSP system and its properties: the transfer of matter from the extended companion to the NS spins it up, decreases its magnetic field, and circularizes the orbit via tidal interactions (T. M. Tauris & E. P. J. van den Heuvel 2023). After the end of this mass transfer, the NS becomes an MSP in different systems like NS–WD binaries, or eclipsing systems like redback or black widow MSPs (see K. Jia & X.-D. Li 2016), all of which have nearly circular orbits.

Interestingly in our case, J1617–2258A does not follow this trend: it is in an ∼18.94 hr compact but highly eccentric ($e \sim 0.54$) binary orbit, which is quite uncommon. In Figure 11, the unique position of this MSP is visible, where there are only four MSPs (three are from the GCs) with orbits more compact and more eccentric than this orbit, but all of them have a median companion mass higher than J1617–2258A's median companion mass.

The reason for J1617–2258A's highly eccentric compact orbit is likely to be past close flybys with other GC stars, which can change the eccentricity of the orbit (e.g., E. S. Phinney 1992). An exchange encounter is also possible, but such encounters generally replace the light companions with more massive objects (P. C. Freire et al. 2004; R. S. Lynch et al. 2012; M. E. DeCesar et al. 2015; E. D. Barr et al. 2024).

5.5.2. Rate of Advance of Periastron

With more than one year of timing baseline, this highly eccentric compact orbit allowed us to detect one post-Keplerian (PK) parameter, the rate of advance of the periastron ($\dot{\omega}$), in our timing with sufficient detection significance. If this is purely relativistic, then in general relativity (GR), this is related to the total mass of the system by

$$\dot{\omega} = 3T_{\odot}^{2/3}\left(\frac{P_{\rm b}}{2\pi}\right)^{-5/3}\frac{M_{\rm tot}^{2/3}}{1-e^2}, \qquad (13)$$

where $M_{\rm tot} = M_{\rm p} + M_{\rm c}$. Our measurement of $\dot{\omega}$ results in $M_{\rm tot} = 1.67 \pm 0.06\,M_{\odot}$.

If we combine the nominal value of the total mass with the mass function equation (given by Equation (9), we obtain for $i = 90°$ a minimum companion mass of 0.072 $M_{\odot}$ and a maximum pulsar mass of 1.60 $M_{\odot}$. A detailed Bayesian statistical approach for the individual mass measurement is done in Section 5.5.3.

5.5.3. Probability Distribution of Pulsar Mass

Given the only measurement of $\dot{\omega}$, and the unavailability of significant detection of other relativistic parameters, in the previous section, we were only able to derive limits on the pulsar and the companion mass based on the total mass of the system. To better quantify the masses and their uncertainties given the constraints of the timing, and to properly include the constraints from the lack of measurement of the Shapiro delay and any other relativistic effects that might be present in the timing with low significance, we make a Bayesian χ^2 map. This samples $\cos i$ and $M_{\rm tot}$ uniformly. For each point in this grid, we calculate $M_{\rm c}$ and then include the values of $M_{\rm tot}$ and $M_{\rm c}$ in a DDGR (J. H. Taylor & J. M. Weisberg 1989) timing solution, where they are kept fixed. This type of orbital model assumes the validity of GR in a self-consistent way and takes into account all relativistic constraints that might be present in the timing. We then use `TEMPO` to obtain the optimal solution for those values, recording the value of χ^2. This is then converted into a 2D probability density function (pdf) using the Bayesian method of E. M. Splaver et al. (2002). We then project this pdf into the $\cos i$–$M_{\rm c}$ and $M_{\rm p}$–$M_{\rm c}$ spaces, and from these we derive the 1D pdfs for $M_{\rm tot}$, $M_{\rm p}$, $M_{\rm c}$, and $\cos i$.

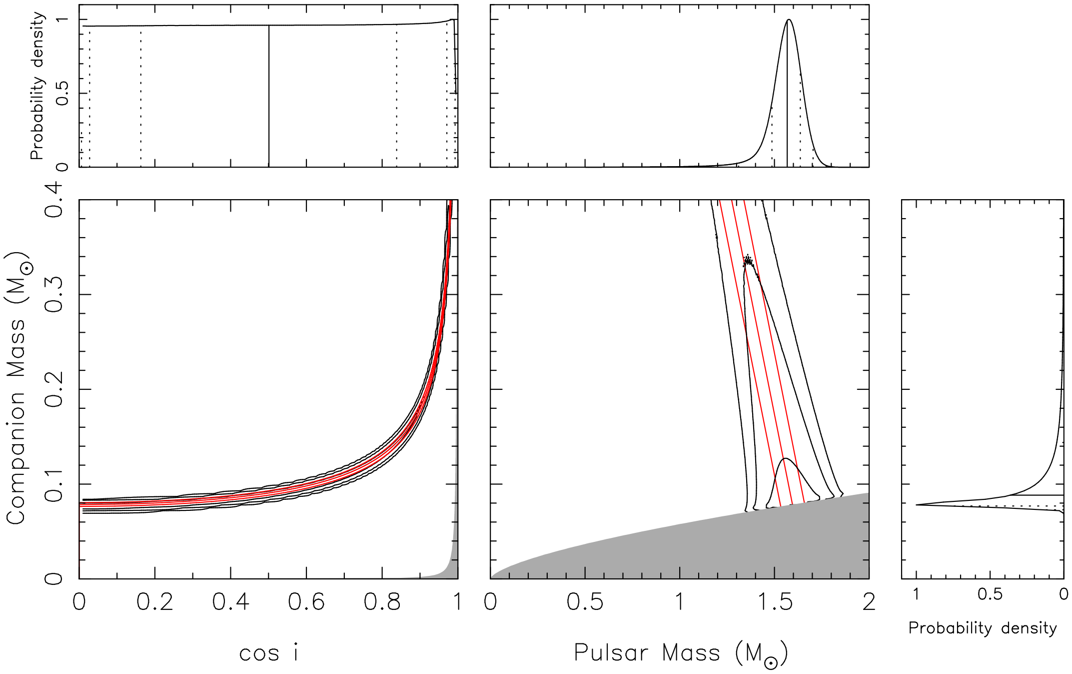

Figure 12. Mass–mass diagram for J1617–2258A. Bottom left panel: $\cos i$–$M_{\rm c}$ space. The gray area is excluded by the requirement that $M_{\rm p} > 0$. Bottom middle panel: $M_{\rm p}$–$M_{\rm c}$ space. The gray area is excluded by the requirement that $\sin i \leqslant 0$. The mass constraints from the measurement of $\dot{\omega}$ are depicted in red. The solid black contours include 68.3%, 95.4%, and 99.7% of all probability in the probability density function (pdf) in each panel. Top left panel: 1D pdf for $\cos i$. Top right panel: 1D pdf for $M_{\rm p}$. Bottom right panel: 1D pdf for $M_{\rm c}$. The solid and dotted lines in these rectangular panels depict the medians and 1σ-, 2σ-, and 3σ-equivalent percentiles.

These 2D and 1D pdfs are depicted in Figure 12. In the square panels, the pdfs are depicted by contours that include 68.3%, 95.4%, and 99.7% of the 2D pdf. In the rectangular panels, we depict the 1D pdfs for $\cos i$, $M_{\rm p}$, and $M_{\rm c}$.

The medians and $\pm 1\sigma$ percentiles of these pdfs are $M_{\rm tot} = 1.672 \pm 0.063\, M_\odot$, $M_{\rm p} = 1.567^{+0.060}_{-0.080}\, M_\odot$, and $M_{\rm c} = 0.086^{+0.056}_{-0.012}\, M_\odot$.

For $\cos i$, we see that the pdf is nearly flat. This means that no other relativistic effects are detected and that at the moment, the individual masses cannot be estimated, other than via the statistical assumption of a flat distribution of $\cos i$.

5.5.4. The Companion and Binary Type

During the timing observation, we roughly sampled every part of the orbit (Figure 10) and for every observation, the MSP was detected at about the expected SNR and no eclipsing phenomenon was observed. In most cases, spider MSPs (redbacks and black widows) show eclipsing due to the interaction of the pulsar pulse with its nondegenerate companion outflows (Z. Yan et al. 2021; S. Kumari et al. 2024). If this MSP system is a spider system then either the eclipsing is covering a very small part of the orbital phase and the region remained unsampled until now or the eclipsing could be frequency dependent, but for that fine sampling of the orbital phase and observation in different frequencies except 550–750 MHz is needed to confirm if it is a spider MSP system.

Another possibility is that the system is not a spider system but rather an NS–WD binary system. For an MSP with a Population I WD companion, according to T. M. Tauris & G. J. Savonije (1999)'s $P_{\rm b}$–$M_{\rm c}$ correlation, for a compact orbit ($P_{\rm b} \sim 1$ day) we can write

$$\frac{M_{\rm c}}{M_\odot} = \left(\frac{P_{\rm b}}{b}\right)^{1/a} + c \tag{14}$$

where $P_{\rm b}$ is in days, $a = 4.50$, $b = 1.2 \times 10^5$, and $c = 0.12$. Putting our $P_{\rm b}$ value into Equation (14), we get $M_{\rm c} = 0.19\, M_\odot$, which would imply $M_{\rm p} = 1.48 \pm 0.6\, M_\odot$ and $i \sim 24°$. If this low orbital inclination is correct, measuring the Shapiro delay in this system will not be possible, which agrees with our previous analysis.

The relatively low companion mass of J1617–2258A is compatible with its current companion being the white dwarf remnant of the star that recycled the pulsar. Further study is needed to determine its companion type.

6. Summary

This paper discusses the Globular Clusters GMRT Pulsar Search (GCGPS) survey. GCGPS has recently started and is currently searching for MSPs in GCs. This survey is designed to search for GC pulsars in the low-frequency range (300–750 MHz). The target selection criteria and observation strategy are optimized to increase discovery potential. The GCGPS survey exploits the uGMRT's Y-shaped array to form two beams with different baseline lengths to optimize sky coverage along with beam sensitivity.

We present the discovery of the first MSP in the GC NGC 6093 (M80). We localize the MSP from imaging of the field as well as from timing solutions at subarcsecond precession. The timing of the MSP reveals that it is in a highly eccentric ($e \sim 0.54$) compact ($P_{\rm b} \sim 18.94$ hr) relativistic binary. Measurement of one PK parameter (advance of the periastron, $\dot{\omega}$) leads to measurement of the total mass of the system ($M_{\rm tot} = 1.67 \pm 0.06\, M_\odot$); this and the mass function imply $M_{\rm c} \geqslant 0.072\, M_\odot$ and $M_{\rm p} \leqslant 1.60\, M_\odot$. The limit on the companion mass is consistent with the companion being a He WD whose progenitor spun up the pulsar, although we cannot exclude the possibility that the system might have formed in an exchange interaction. There are only four such systems that are more compact and eccentric than this system, but all have a higher median companion mass than this system.

Acknowledgments

We acknowledge the support of the Department of Atomic Energy, Government of India, under project No. 12-R&D-TFR5.02-0700. The GMRT is run by the National Center for Radio Astrophysics of the Tata Institute of Fundamental Research, India. We thank the uGMRT operators for their coordinated effort in conducting the GCGPS survey observations. P.C.C.F. gratefully acknowledges continuing support from the Max-Planck-Gesellschaft and the hospitality of the Academia Sinica Institute of Astronomy and Astrophysics in Taipei, Taiwan, where part of this work was conducted while he was a Visiting Scholar. We also acknowledge support from the Building Indo-UK Collaborations towards the Square Kilometre Array program, which facilitated the development of the pulsar search pipeline, particularly the highly efficient GPU-based version. We also thank our anonymous referee for insightful comments, which helped make the necessary corrections.

ORCID iDs

Jyotirmoy Das https://orcid.org/0009-0006-7995-5871
Jayanta Roy https://orcid.org/0000-0002-2892-8025
Paulo C. C. Freire https://orcid.org/0000-0003-1307-9435
Scott M. Ransom https://orcid.org/0000-0001-5799-9714
Bhaswati Bhattacharyya https://orcid.org/0000-0002-6287-6900
Karel Adámek https://orcid.org/0000-0003-2797-0595
Wes Armour https://orcid.org/0000-0003-1756-3064
Sanjay Kudale https://orcid.org/0000-0002-6631-1077
Mekhala V. Muley https://orcid.org/0009-0008-1233-6915

References

Abbate, F., Ridolfi, A., Barr, E. D., et al. 2022, MNRAS, 513, 2292
Abbate, F., Ridolfi, A., Freire, P. C. C., et al. 2023, A&A, 680, A47
Abdo, A. A., Ackermann, M., Ajello, M., et al. 2010, A&A, 524, A75
Bahramian, A., Heinke, C. O., Sivakoff, G. R., & Gladstone, J. C. 2013, ApJ, 766, 136
Barr, E. D., Dutta, A., Freire, P. C. C., et al. 2024, Sci, 383, 275
Becker, W., & Trümper, J. 1999, A&A, 341, 803
Bhat, N. D. R., Cordes, J. M., Camilo, F., Nice, D. J., & Lorimer, D. R. 2004, ApJ, 605, 759
Bhattacharyya, B., Cooper, S., Malenta, M., et al. 2016, ApJ, 817, 130
Bhattacharyya, B., Roy, J., Stappers, B. W., et al. 2019, ApJ, 881, 59
Bogdanov, S., van den Berg, M., Servillat, M., et al. 2011, ApJ, 730, 81
Camilo, F., Lorimer, D. R., Freire, P., Lyne, A. G., & Manchester, R. N. 2000, ApJ, 535, 975
Chen, J., Cadelano, M., Pallanca, C., et al. 2023, ApJ, 948, 84
Cordes, J. M., & Lazio, T. J. W. 2002, arXiv:astro-ph/0207156
Corongiu, A., Ridolfi, A., Abbate, F., et al. 2024, ApJ, 972, 198
D'Amico, N., Possenti, A., Manchester, R. N., et al. 2003, in ASP Conf. Ser. 302, Radio Pulsars, ed. M. Bailes, D. J. Nice, & S. E. Thorsett (San Francisco, CA: ASP), 375
Damour, T., & Deruelle, N. 1986, AIHPA, 44, 263
DeCesar, M. E., Ransom, S. M., Kaplan, D. L., Ray, P. S., & Geller, A. M. 2015, ApJL, 807, L23
Dewey, R. J., Taylor, J. H., Weisberg, J. M., & Stokes, G. H. 1985, ApJL, 294, L25
Douglas, A., Padmanabh, P. V., Ransom, S. M., et al. 2022, ApJ, 927, 126
Freire, P. C., Gupta, Y., Ransom, S. M., & Ishwara-Chandra, C. H. 2004, ApJL, 606, L53
Freire, P. C. C., Abdo, A. A., Ajello, M., et al. 2011, Sci, 334, 1107
Freire, P. C. C., Hessels, J. W. T., Nice, D. J., et al. 2005, ApJ, 621, 959
Freire, P. C. C., Ransom, S. M., Bégin, S., et al. 2008, ApJ, 675, 670
Freire, P. C. C., & Ridolfi, A. 2018, MNRAS, 476, 4794
Freire, P. C. C., Ridolfi, A., Kramer, M., et al. 2017, MNRAS, 471, 857
Freire, P. C. C., & Wex, N. 2024, LRR, 27, 5
Gautam, T., Ridolfi, A., Freire, P. C. C., et al. 2022, A&A, 664, A54
Gupta, Y., Ajithkumar, B., Kale, H. S., et al. 2017, CSci, 113, 707
Hankins, T. H. 1971, ApJ, 169, 487
Harris, W. E. 1996, AJ, 112, 1487
He, Q., & Shi, X. 2024, MNRAS, 527, 5183
Hessels, J. W. T., Ransom, S. M., Stairs, I. H., Kaspi, V. M., & Freire, P. C. C. 2007, ApJ, 670, 363
Jia, K., & Li, X.-D. 2016, ApJ, 830, 153
Johnson, T. J., Guillemot, L., Kerr, M., et al. 2013, ApJ, 778, 106
Kale, R., & Ishwara-Chandra, C. H. 2021, ExA, 51, 95
Kudale, S., Roy, J., Chengalur, J. N., Sharma, S., & Kumari, S. 2024, ApJ, 972, 61
Kumari, S., Bhattacharyya, B., Sharan, R., et al. 2024, ApJ, 973, 19
Li, B., Zhang, L.-y., Yao, J., et al. 2024, ApJ, 962, 43
Lian, Y., Freire, P. C. C., Cao, S., et al. 2025, ApJL, 981, L3
Lian, Y., Pan, Z., Zhang, H., et al. 2023, ApJL, 951, L37
Lorimer, D. R., & Kramer, M. 2004, Handbook of Pulsar Astronomy, Vol. 4 (Cambridge: Cambridge Univ. Press)
Lynch, R. S., Freire, P. C. C., Ransom, S. M., & Jacoby, B. A. 2012, ApJ, 745, 109
Lynch, R. S., Ransom, S. M., Freire, P. C. C., & Stairs, I. H. 2011, ApJ, 734, 89
Manchester, R. N., Hobbs, G. B., Teoh, A., & Hobbs, M. 2005, AJ, 129, 1993
McKinnon, M. M. 2014, PASP, 126, 476
McMillan, P. J. 2017, MNRAS, 465, 76
Padmanabh, P. V., Ransom, S. M., Freire, P. C. C., et al. 2024, A&A, 686, A166
Pan, Z., Ma, X.-Y., Qian, L., et al. 2021b, RAA, 21, 143
Pan, Z., Qian, L., Ma, X., et al. 2021a, ApJL, 915, L28
Park, R. S., Folkner, W. M., Williams, J. G., & Boggs, D. H. 2021, AJ, 161, 105
Phinney, E. S. 1992, RSPTA, 341, 39
Pooley, D., Lewin, W. H. G., Anderson, S. F., et al. 2003, ApJL, 591, L131
Possenti, A., D'Amico, N., Corongiu, A., et al. 2005, in ASP Conf. Ser. 328, Binary Radio Pulsars, ed. F. A. Rasio & I. H. Stairs (San Francisco, CA: ASP), 189
Possenti, A., D'Amico, N., Manchester, R. N., et al. 2001, arXiv:astro-ph/0108343
Prša, A., Harmanec, P., Torres, G., et al. 2016, AJ, 152, 41
Ransom, S. M., Hessels, J. W. T., Stairs, I. H., et al. 2005, Sci, 307, 892
Ransom, S. M., Stairs, I. H., Backer, D. C., et al. 2004, ApJ, 604, 328
Reddy, S. H., Kudale, S., Gokhale, U., et al. 2017, JAI, 6, 1641011
Ridolfi, A., Freire, P. C. C., Gautam, T., et al. 2022, A&A, 664, A27
Ridolfi, A., Gautam, T., Freire, P. C. C., et al. 2021, MNRAS, 504, 1407
Sarazin, C. L., Kundu, A., Irwin, J. A., et al. 2003, ApJ, 595, 743
Shklovskii, I. S. 1970, SvA, 13, 562
Singleton, J., DeCesar, M., Dai, S., et al. 2024, arXiv:2412.11271
Splaver, E. M., Nice, D. J., Arzoumanian, Z., et al. 2002, ApJ, 581, 509
Swarup, G., Ananthakrishnan, S., Kapahi, V. K., et al. 1991, CSci, 60, 95
Tam, P.-H. T., Hui, C. Y., & Kong, A. K. H. 2016, JASS, 33, 1
Tam, P. H. T., Kong, A. K. H., Hui, C. Y., et al. 2011, ApJ, 729, 90
Tauris, T. M., & Savonije, G. J. 1999, A&A, 350, 928
Tauris, T. M., & van den Heuvel, E. P. J. 2023, Physics of Binary Star Evolution. From Stars to X-ray Binaries and Gravitational Wave Sources (Princeton, NJ: Princeton Univ. Press)
Taylor, J. H., & Weisberg, J. M. 1989, ApJ, 345, 434
Vasiliev, E., & Baumgardt, H. 2021, MNRAS, 505, 5978
Verbunt, F., & Freire, P. C. C. 2014, A&A, 561, A11
Verbunt, F., & Hut, P. 1987, in IAU Symp. 125, The Origin and Evolution of Neutron Stars, ed. D. J. Helfand & J. H. Huang (Cambridge: Cambridge Univ. Press), 187
Vleeschower, L., Corongiu, A., Stappers, B. W., et al. 2024, MNRAS, 530, 1436
Wang, L., Peng, B., Stappers, B. W., et al. 2020, ApJ, 892, 43
Webb, N. A., Wheatley, P. J., & Barret, D. 2006, A&A, 445, 155

Wu, Y., Pan, Z., Qian, L., et al. 2024, ApJL, 974, L23
Yan, Z., Pan, Z.-c., Ransom, S. M., et al. 2021, ApJ, 921, 120
Yao, J. M., Manchester, R. N., & Wang, N. 2017, ApJ, 835, 29
Yin, D., Zhang, L.-y., Qian, L., et al. 2024, ApJL, 969, L7
Zhang, L., & Cheng, K. S. 2003, A&A, 398, 639
Zhang, L., Freire, P. C. C., Ridolfi, A., et al. 2023, ApJS, 269, 56
Zhang, P., Xing, Y., & Wang, Z. 2022, ApJL, 935, L36
Zhou, D., Wang, P., Li, D., et al. 2024, SCPMA, 67, 269512